Micromachined silicon grisms for infrared optics

D. J. Mar, J. P. Marsh, D. T. Jaffe

Department of Astronomy, The University of Texas at Austin, 1 University Station, Austin, TX 78712-0259

We demonstrate the successful fabrication of large format (50 mm × 50 mm) gratings in monolithic silicon for use as high-efficiency grisms at infrared wavelengths. These devices are fabricated from thick (8-16 mm) oriented single-crystal silicon substrates using microlithography and wet chemical etching techniques. Characteristics of these grisms include coarse grooves, high refractive index, precise control of the blaze angle and groove profile, and excellent groove surface quality. Measurements of the structure of the gratings confirm that the physical dimensions of the final devices closely match their design values. In infrared wavelength regions where silicon transmits well, the blaze control and high-index permit high-resolution, high-order dispersion in a compact space. Detailed measurements of the optical performance of these devices demonstrate that they exceed the specifications required for efficient diffraction-limited performance in the near and mid-infrared (1-30 microns). Peak diffraction efficiencies measured in reflection compare favorably with those of ruled or

replicated gratings in other materials. Transmission tests of our grisms confirm excellent performance in the infrared. In a first application, we have used these grisms to provide a mid-infrared camera with a moderate resolution (R = 100-1000) spectroscopic capability.

OCIS codes: 050.1950, 300.6340, 350.1260

1. Introduction

Transmission gratings mounted on or fabricated on wedged substrates combine the dispersive action of a diffraction grating with the varying optical path length across the prism, and are therefore called grisms, or Carpenter prisms. Typically, grisms are inserted into a beam of collimated or nearly collimated optical or infrared light and used to disperse the light as it is transmitted through the device. The primary geometrical parameters are the grism wedge angle δ and the grating period σ; these specify into which angles the various wavelengths and orders are diffracted. The grating equation applied to a grism in which the blaze angle is equal to the wedge angle δ is

$$\frac{m\lambda}{\sigma} = n\sin\left[\delta - \sin^{-1}\left(\frac{\sin\alpha}{n}\right)\right] + \sin\beta, \tag{1}$$

where m is the order in which the grating is used, λ is the vacuum wavelength, and n specifies the index of refraction of the grism material. The angle δ is the prism wedge

angle, and α and β specify the angles of the incident and transmitted beams with respect to the normals at the entrance and grating (exit) faces of the prism (see Figure 1). A beam that passes through without deflection satisfies $\beta = \alpha - \delta$, and Eq. 1 becomes

$$m\lambda/\sigma = n \sin\{\delta - \sin^{-1}[(\sin \alpha)/n]\} + \sin(\alpha - \delta). \quad (2)$$

For grisms that are blazed such that the facets are parallel to the entrance face, the blaze wavelength condition occurs when $\delta = \beta$:

$$\frac{m\lambda_{blaze}}{\sigma} = (n-1)\sin\delta, \quad (3)$$

and light at the blaze wavelength passes through the grism undeviated. For modest angle grisms ($\delta < 40°$) used in low order, reasoning from scalar electromagnetic theory predicts a maximum in the efficiency at wavelengths near λ_{blaze}, although for larger δ a more rigorous treatment may be necessary.[1] The diffraction-limited resolving power for nearly normal incidence ($\alpha \approx 0$) is given by

$$R = \frac{\lambda}{\Delta\lambda} = (n-1)\ \tan\delta\ \frac{D}{\lambda}, \quad (4)$$

where D is the pupil diameter. For a given wavelength λ and resolving power R, D is inversely proportional to $n - 1$. Thus, the size of the pupil (and that of the overall optical system) can be reduced by selecting grisms made from high index material rather than low index material. Equivalently, for a given D/λ ratio, the resolving power is increased by choosing a material with a high refractive index (see Table 1), or by going to larger

grism angles. It is possible to relax the condition that the blaze facets be parallel to the entrance face, so that the wedge angle δ and the blaze angle θ are not necessary equal (see left panel of Fig. 1) and the undeviated beam is no longer on the blaze. This geometry can be used to reduce the projection of the beam upon the unused facets to minimize geometric shadowing losses (see Section 4), but only at the cost of an increase in the overall thickness of the device.

The grating side of a grism is a periodic array of diffracting elements, and is usually formed by one of four methods: ruling, replication, diamond-machining or patterning/etching. For visible wavelengths, ruled gratings in glass or replica gratings in resin that can be mounted on prisms are commercially available.[2,3] At longer wavelengths, however, optical transmission properties can limit the choice of material, as most resins become absorbing beyond about 3 μm. Also, the groove spacing of an infrared grating is typically larger than that for a visible light grating by about a factor of 3 to 10. This coarseness can preclude the selection of ruled grisms, as it is difficult to control the blaze when removing large amounts of substrate material. Diamond-machining techniques (Davies et al. 2003, Kuzmenko 2006) can generate both intricate and coarse structures[4,5] on many substrates (including metals, Si, ZnSe, Ge, and many polymers) with very low surface roughness (~5 nm), but the surface may still possess long-wavelength machining defects such as cutting arcs and ripple. For large-area gratings, issues can arise with cutting tip wear, due to the serial way in which each groove is created. This serial process is relatively slow and therefore places demands on the thermal and mechanical stability during machining. An alternative fabrication method

using lithography and anisotropic etching is, by contrast, a parallel method. These processes can produce coarser groove spacings with excellent blaze characteristics and surface quality. They are particularly suited for single-crystal materials in which the crystalline directions are maintained throughout the entire substrate. In this work we focus on near and mid-infrared applications using silicon (see Section 2).

In optical applications, grisms are often used as compact dispersers that do not appreciably deviate the direction of a collimated beam at the blaze wavelength. From Eq. 1 it can be shown that

$$\sin\beta = \frac{m\lambda}{\sigma} - n\sin\delta + \sin\alpha\cos\delta + O\left(\frac{\sin\alpha}{n}\right)^2. \tag{5}$$

This implies that small misorientations of the grism are not catastrophic.[6] For example, for a Si grism with n = 3.4, δ = 6.16°, and σ = 87 μm operating at m = 1, a device tilt of 1° in the dispersion axis leads to a deflection of the central blaze wavelength of less than 0.001°. It can also be shown from Eq. 1 that $d\beta/d\lambda$ is approximately constant with small changes in incidence angle $\Delta\alpha$. Since the transmitted light through a grism is not very sensitive to the angular orientation of the device, grisms may be mounted in filter wheels or similar inexpensive mechanisms that do not have extremely tight tolerances on the angular positioning.

Because the light rays pass through the grism undeviated or nearly so, downstream optics can support both imaging and spectroscopic modes, depending on whether the grisms are in the path of the beam or not. The use of grisms can thereby

simplify the design of a multifunction instrument. They therefore have found a place in many near-infrared[7-9] and mid-infrared[10-12] astronomical spectrographs. Other potential applications for grisms include dispersion of wavelength-multiplexed light signals into an array of beams, thereby providing simultaneous demultiplexing with a "single grating coupler" element instead of a bank of filters for optical communication in the near-IR[13,14] or confocal microscopy[15,16] at visible wavelengths. Another potential application uses combinations of grisms to compensate higher order dispersive effects when compressing and stretching light pulses, a technique that makes them potentially useful for time-domain laser pulse applications.[17,18]

The work here demonstrates the fabrication of high quality silicon grisms with coarsely spaced grooves for near and mid-infrared spectroscopy applications (see Table 2). We discuss the choice of silicon as a suitable material, report on the techniques and methods used to fabricate the grisms, discuss factors that can limit their performance, and display finished devices that have high efficiency over large (2.5 cm and up) aperture diameters. As a direct consequence, the grisms exhibited here will provide a mid-infrared camera on an airborne astronomical observatory with moderate resolution spectroscopy capabilities. Large, coarsely-ruled silicon grisms may be combined in cross-dispersed configurations to enable a new capability: moderate to high-resolution spectroscopy in the near-IR using all-transmissive optics. In a companion paper,[19] we discuss the production and evaluation of high quality silicon gratings as reflection devices used in immersion.

2. Silicon

Silicon is an important and useful optical material both because of its optical and mechanical properties and because process technologies have been developed for semiconductor VLSI electronics and MEMS applications. As shown in Fig. 2, high-purity silicon transmits well from 1.2 to ~8 μm and from 20 to 27 μm.[20-23] Between these regions, infrared lattice absorption is observed[24] and limits usable optical path lengths to a few mm or less. By using high-resistivity (ρ > 1000 ohm-cm) float-zone silicon, for which the absorption coefficient can be small (e.g. $\alpha < 10^{-2}$ cm^{-1} for λ between 1.2 and ~6 μm,[22,23] and by insuring that the fabrication process neither creates excessive damage to the silicon lattice nor introduces impurities that can scatter light, the absorption losses can be kept at the few percent level. Except for particularly strong absorption near 16 μm, the lattice absorption can be reduced by lowering the temperature. Narrow and strong absorption features due to oxygen may occur near 9 μm and 19 μm.[25-27] For infrared applications from 1 to 40 μm, lower oxygen content reduces these absorptions (see Figure 2). Other absorption features occur to 40 μm.[28] The short wavelength cutoff occurs at a wavelength of approximately 1.1 to 1.2 μm[29,30] at the silicon bandgap. At lower temperatures the cutoff moves slightly towards shorter wavelengths (~1.07 μm at 77 K). For silicon diffraction gratings that are fabricated using wet-etch processes to create the diffracting surfaces, a low oxygen content also reduces the facet roughness,[31,32] although it is not clear that the surface roughness of the facets is the dominant scattering process.[33] The high index of refraction of silicon (n = 3.44 at λ = 2.5 μm at 295 K) [34] permits large dispersing power in a small device, as the resolving power in Eq. 4 can be

larger by a factor of 5 than for a grism made from modest index material such as CaF_2 or from a resin. The optical index decreases by approximately 0.8% as the temperature is lowered from 295 K to 80 K.[34] Mechanically, silicon is hard, possesses a high elastic modulus, and can be polished to high optical flatness. It is vacuum-compatible and its optical transmission in the near-infrared improves slightly with decreasing hydrostatic pressure.[35] When cooled to the cryogenic temperatures required for sensitive infrared optical measurements, it is mechanically stable and has a modest thermal contraction relative to those of metals and other mounting materials. It is possible to apply antireflection coatings to silicon surfaces to enhance the transmission at the silicon-vacuum (or silicon-air) interfaces.

Fabrication of diffraction gratings in silicon exploits lithographic processes that have been developed for industrial applications. The patterning of precisely positioned periodic grooves can be accomplished by photolithography methods[36] that permit precise pattern transfer onto a silicon surface that has been polished optically flat. In combination with anisotropic wet-etch techniques that preferentially etch along the ⟨100⟩ directions hundreds of times faster than along the ⟨111⟩ directions,[37,38] lithographic patterning permits the fabrication of precisely positioned and aligned {111} facets in the grating surface.[39] Control of the groove orientation is achieved by the underlying atomic structure. For single crystal silicon, the orientation of the grooves is essentially perfect. The high etch anisotropy leads to groove profiles that are flat and smooth from the groove top to the valley (see Fig. 3).

3. Fabrication

Over the past decade, several groups have developed methods for fabricating diffraction gratings on silicon substrates.[40-49] Substrates that are considerably thicker than standard semiconductor wafers require modifications to semiconductor processing methods. We have developed methods to produce gratings with asymmetric groove profiles (see Figure 3), a necessary step for the production of low-order grisms.[47] We have been successful in producing high-quality gratings on monolithic substrates, thus producing grisms designed for use between 5 and 38 μm (but suitable for use at 1.1-5 μm as well) that are complete (see Figure 4) except for commercial anti-reflection coating. Our fabrication methods are summarized in this section.

Our production starts from blanks of high-purity monocrystalline silicon. Silicon is commercially available as boules of various diameters (e.g. 100 mm, 150 mm, 200 mm) and resistivities. During wet-etch processes, crystal defects can produce pits and hillocks[50] that can scatter light in optical applications. Such issues, as well as the preference for low-oxygen content, have led us to select float-zone (FZ) material. Knowledge of the crystal growth axis of commercial silicon boules is accurate to approximately 1°. In lithographic patterning alignment steps, this level of accuracy is insufficient to prevent dislocations from appearing during the chemical micromachining of long grooves. We therefore orient the boule by using x-ray diffractometry to locate the crystal directions to within 0.05°. A precision (110) flat is then ground on one side of the boule. This flat is perpendicular to the grating surface and to the groove facets (see Figure 1) and serves two purposes: it provides a stable platform upon which to mount the

boule for subsequent cutting, and it serves as an alignment marker in later lithographic steps. The boule is then sliced into blanks of sufficient thickness (typically 10-20 mm) to contain the grisms and to guarantee their rigidity. The blaze angle θ is determined by bias-slicing the boule at the appropriate angle. For example, if the surface exposed by the slice is a (100) plane, a symmetric (θ = 54.7°) grating will result (center panel of Figure 3), whereas rotating the boule around the ⟨210⟩ axis produces gratings with asymmetric groove profiles (top and bottom panels of Fig. 3). The exposed surfaces are then ground, etched to remove saw damage, and the top surface is polished to optical flatness (typical root mean square (rms) surface figures less than 1/50 wave at 632.8 nm) using chemical-mechanical planarization (CMP) processes. This results in an extremely flat surface (while minimizing mechanical stresses at and near the surface.[51] The blanks are then coated with a thin (60-100 nm) film of low pressure chemical vapor deposition (LPCVD) silicon nitride as a passivation layer.

At this point, we create a series of regularly spaced lines on the nitride layer using photolithography. Many of the lithography steps are described elsewhere[42,43,45,47] and additional details of our current process are available in Ref. 19. Our lithographic process employs a positive photoresist that is flood-illuminated by g-line (436 nm) and i-line (365 nm) light from a mercury-gallium lamp. To spin-coat the photoresist onto the massive blanks, we employ a custom-built spin table with sufficient torque to spin the combined moment of inertia of the blank and holder up to several thousand rpm in a period of a few seconds. Once the photoresist has been cured by heating the blank to approximately 100°C for 20 min, a chrome-on-quartz mask containing the negative of the

desired grating pattern is carefully placed in contact with the photoresist layer. The flood illumination through the mask transfers the mask pattern to the photoresist layer. The exposure system is a custom designed apparatus that can accommodate a wide range of substrate thicknesses (0.5 to 35 mm). During the exposure step, the temperature of the silicon blank and the quartz mask are held to within a few °C across the grating, thereby preventing potential pattern transfer errors arising from the different thermal expansions of the substrate and mask.

After the photoresist has been exposed, an image of the mask pattern is produced in the photoresist layer by immersing the photoresist-coated blank in a commercial developer solution. Next, the nitride layer is patterned using a dry (plasma) etch. The photoresist layer serves as an etch mask during this step. Thick substrates undergoing plasma etching can display nonuniform etching, due to variations in the electric field profile and in the plasma density within a reactive ion etch (RIE) chamber that is normally used to process thin semiconductor wafers. We have modified our plasma etcher to maintain uniformity of the plasma in contact with the patterned surface. After the dry etch, the photoresist is stripped by immersion in acetone. The groove facets themselves that form the grating are then created by anisotropic etching in an aqueous solution of potassium hydroxide and isopropanol, maintained at 68ºC by immersion in a recirculating water bath. Ultrasonic vibrations assist in detaching bubbles from the etched surface.

Etching in potassium hydroxide creates a blazed grating over the entire patterned area of the silicon surface. A photograph of a processed blank is shown in the top panel

of Figure 4 and scanning electron microscope (SEM) micrographs of micromachined silicon gratings are shown in Figures 3 and 5. The nitride strips that protected the groove tops (see Figure 5) during anisotropic etching are removed by immersing the grating in hot concentrated phosphoric acid at 140ºC or more. Removal of the nitride promotes adhesion of antireflection coatings that are subsequently applied to the grating surface.

To form a complete grism, the blank is cut into the desired prism shape. For the devices discussed in this paper, the entrance faces are formed parallel to the grating facets ($\delta = \theta$). These faces are optically polished to high flatness, with final surface figures less than ~1/20 of a wave rms at 632.8 nm. These devices are now complete (see center and bottom panels in Figure 4) except for anti-reflection coating on the entrance and grating of the prism.

4. Factors affecting grating performance

For applications such as infrared spectrographs, which demand high sensitivity to faint sources, overall efficiency is a primary consideration. As light passes through the grism substrate and is diffracted by the grating, it is subject to losses that can limit the ideal optical performance of the grating: index mismatch loss at the entrance and exit faces, geometric losses, absorption and scattering within the bulk, scattering at the surface, and various types of groove errors.[52] In this section we describe these potential sources of error and their possible effects on the grating performance.

Index mismatch losses (or Fresnel losses) take place at interfaces where there is a discontinuity in the index of refraction. Because the index of silicon is large (n = 3.4), the substantial reflection loss at the two interfaces limits the transmission of an uncoated

silicon device to $[4n/(n + 1)^2]^2 = 49\%$. By applying broadband anti-reflection optical coatings to the entrance and exit faces of the silicon grism, the transmission can be raised to ~95%. Applying uniform multilayer coatings to the corrugated surfaces of a grating can be challenging, but it is possible.[53]

Losses occur where portions of the beam area are geometrically shadowed by parts of the grism grooves. For a normally-incident ($\alpha = 0$) beam from the left, most of the light passes through the vertical facet and is diffracted according to Eq. 1. However, at the top and bottom of each vertical facet, the shorter sloping facet and the groove top τ intercept a fraction of the beam (see Fig. 1, center). Depending on the value of α and on the details of the groove geometry, this light is diffracted into other directions and thereby lost. In the case of normal incidence and with the blaze parallel to the entrance face ($\delta = \theta$), the loss is minimized by using valley angles near 90° and keeping the groove top τ as short as possible. Figure 6 shows this geometrical loss as a function of grism angle δ, for $\delta = \theta$ and a fixed ratio $\tau/\sigma = 0.05$. A full electromagnetic calculation can be done to model the efficiency behavior of grisms in low order. The valley angle depends on the material and on the processing steps used to fabricate the grism. For silicon, it is possible to produce valley angles of either 70.53° or 109.47° depending on the crystal orientation.[47] Figure 6 shows that the choice of 70.53° is preferable, since in that case the areas lost to the unused facet and to the groove top partially coincide and therefore sustain less shadowing loss.

Scattering and absorption within the bulk silicon can also lower the optical throughput. To minimize these bulk effects, the optical path length through the material

should be kept as short as possible. The optical path length difference across the beam is the product of the beam diameter and $n\tan\delta$. Some additional substrate thickness is required to prevent flexure. Processing silicon at elevated temperatures around 800-1000 °C appears to be beneficial in reducing the infrared activity of oxygen defects;[26] in our case, this processing is achieved incidentally during the deposition of the LPCVD nitride layer. Because the grism is a wedged device, differential bulk absorption/scattering occurs across the aperture. The linearly varying path length through the wedge results in an intensity that tapers exponentially across the grating and slightly broadens the point spread function in the direction of the taper, thus reducing the contrast in the sidelobe pattern. As illustrated in Figure 7, these effects are negligible.

Light can be scattered from imperfections at the grating surface. Some of these defects are randomly distributed, such as point defects and surface roughness. Leftover silicon nitride and other debris on the surface (see bottom panel of Figure 5) can also contribute to scattering. To assess the surface condition of the gratings on nanometer length scales, we use atomic force microscopy (AFM). Figure 8 shows an AFM scan of a 5 μm × 5 μm portion of a groove facet of grism with $\theta = 6.16°$ and $\sigma = 25$ μm (G2, see Table 2). As shown, the grooves are smooth: the surface roughness is less than 2 nm rms and the groove facet is free from hillocks and etch pit formations.[50,53] Even if the grooves themselves are smooth (Figure 8) and flat (Figure 3), the overall grating performance can be degraded by any errors in the groove orientations and locations. Orientation errors are unlikely since the groove facets are aligned with the underlying silicon lattice, which is monocrystalline. Piston-type groove errors due to variations in

groove placement may originate from noise sources associated with lithography. Jog defects—abrupt changes in displacement within a single groove—most likely arise from irregularities in the width of the nitride lines that are patterned by the plasma etch. If these jog displacements are large compared with the wavelength, they lead to inter-order power in the blaze. To eliminate such defects, we modified the plasma etcher to homogenize the electric field and plasma density, resulting in jog defect densities below 10 cm^{-2} and areal fractions under 0.1%.

Assuming that the groove position errors are Gaussian and uncorrelated, the grism optical path error is

$$\varepsilon = (n - 1)\, \varepsilon_{rms} \tag{6}$$

where ε_{rms} measures the rms "piston" error distribution of the grooves along the optical path. The errors degrade the peak efficiency in the following Strehl expression:

$$\frac{\eta}{\eta_0} = \exp\left[-\left(\frac{2\pi}{\lambda}(n - 1)\varepsilon_{rms}\right)^2\right] \tag{7}$$

where η_0 is the maximum possible efficiency. To maintain at least 80% of the incident power in a diffraction-limited spike, Eq. 7 implies that in silicon (n = 3.4), the rms error tolerance ε_{rms} must be no more than $\lambda/32$, where λ is the vacuum wavelength of the incident beam. If the silicon grating is used as a front surface reflective device in Littrow, the corresponding expression to Eq. 6 for the optical path errors is $\varepsilon_o = 2\varepsilon_{rms}$ and the corresponding 80% criterion is similar: $\varepsilon_{rms} < \lambda/27$. Measured along the grating

surface in the dispersion direction, the actual tolerances in the groove positions are equal to $\varepsilon_{rms}/(\sin\delta)$, so tolerances on groove positioning are less stringent for small grating angles. For a given wavelength, the positioning tolerances for a grism are more forgiving by a factor of $[2n/(n - 1)](\sin\delta_{immersion})/(\sin\delta_{grism})$ than for the tolerances of an immersion grating.[19] The groove position errors can be a combination of both Gaussian random errors and slow variations over longer spatial wavelengths. These long-wavelength errors could be introduced by various steps in the lithography, such as imperfectly flat substrates, imperfect contact between the lithography mask and the substrate, non-uniformity during the plasma etch, or variations in the wet etch environment.[52]

5. Performance Measurements

To establish the extent to which the various sources of error could affect the optical performance, we evaluate our fabricated silicon grisms by a combination of methods, including atomic force microscopy (AFM), scanning electron microscopy (SEM), surface profilometry, and visible and near-infrared optical measurements taken in reflection and transmission. The information gained is fed back into the development to improve the yield and the quality of the finished gratings.[54] Many groove error sources have been eliminated and those that remain are very small. In this section we will demonstrate the excellent optical performance of our fabricated grisms and discuss what the results imply for the geometric, bulk, surface, and groove errors loss mechanisms discussed above.

The geometrical profile of the grooves across the surface is very good. From AFM and SEM scans, we know that the groove facets are smooth (Figures 3 and 8). Using surface profilometry and SEM micrographs of etch undercut, we measure valley

angles of 72.12º, with the profilometry measurement uncertainty being 0.05º. This value is close to the ideal value of $\cos^{-1}(1/3) = 70.53°$ formed by the intersection of adjacent {111} families of crystal planes. The difference in angle results from the finite anisotropy ratio of the etch rates in the ⟨111⟩ and ⟨100⟩ crystal directions which leads to a global tilt of the grating facets. Although finite, the anisotropy ratio is large (~60) and nearly constant, leading to groove facets that are smooth, flat, and parallel to each other. If the anisotropy is known in advance, one should account for the tilt at the orientation step in the processing. Absolute control of the blaze angle is particularly important at low orders for properly setting the blaze wavelength, as can be seen from Eq. 3. Uniformity of the blaze across the grating is important for any optical application.

To evaluate the transmission performance of these grisms, we illuminate them with a collimated beam of λ = 1523 nm laser light and then focus the diffracted beams onto an InGaAs focal plane array. The beam diameter is limited to 10 mm by our test equipment. By suitable choices of the camera focal ratio, we can obtain a point spread function (PSF) by measuring the shape of a single diffraction order (Figure 9), or we can estimate the device throughput by imaging a series of adjacent orders (Figure 10). Figure 9 shows the normalized one-dimensional PSF of grism G3 ($\theta = 32.6°$, σ = 87 µm, and τ = 6.0 µm, see Table 2). As shown, the shape and width of the diffraction spots are virtually identical to those obtained for a flat mirror and agree with the theoretical curve for a circular aperture, verifying diffraction-limited performance over the beam aperture. The measured full width of the profile corresponds to a resolving power of 10^4. Before normalizing the PSFs, the peak value of the grism PSF is ~25% of that measured for the

mirror. Figure 10 shows transmission spectra for grisms G3, G4, and G5. These data were obtained using the same beam (10 mm diameter, λ = 1523 nm) as for Figure 9, but the camera optics are faster and the field-of-view correspondingly greater. Each of the spectra in Figure 10 consists of a series of orders, because the laser wavelength is not on the blaze for these grisms. Between orders, no ghosts are visible in Fig. 10, and in high signal-to-noise measurements, we have verified their absence down to a level of $<10^{-3}$ of the brightest order.[19] By summing up the power in the series of orders, we measure the efficiencies listed in Table 3. The raw efficiency η_{raw} is simply the ratio of power in the observed diffraction orders to the power incident on the entrance face, and should be nearly equal to the efficiency on the blaze. Since the grisms are not yet equipped with anti-reflection coatings, the raw transmission cannot exceed the value permitted by index mismatch (49%).

The groove efficiency η_{groove} corrects the measured efficiency η_{raw} for all effects related to the grism geometry and the optical application, but not for effects arising from any groove positioning or blaze imperfections. It assesses the quality of the grooves alone. For the values of η_{groove} in Table 3, we normalize η_{raw} by factors that account for the geometric loss (see Fig. 6), and for the dielectric mismatch between the uncoated silicon and air. It is also possible to account for the diffracted power in peaks that are not directly imaged.[19] For the three devices in Table 3, we estimate the magnitude of this factor at 1-2%, but do not include it explicitly, leading to conservative values for η_{groove}. As the groove efficiencies are nearly 100% of the theoretical maximums permitted by

geometric and index mismatch limitations, this indicates that the grisms are of excellent optical quality.

This picture is strengthened by external reflection measurements using light at λ = 543.5 nm, 632.8 nm, and 1523 nm. In Figure 11 we show reflection spectra taken using a collimated 25 mm beam from a green HeNe laser with λ = 543.5 nm. Since this wavelength is not on the blaze for any of the grisms shown, the incident beam is diffracted into multiple orders. As before, no diffraction ghosts are visible between the orders. By summing up the power in the series of orders, we can obtain an estimate of the on-blaze efficiency. For the three spectra in Figure 10, these reflection efficiencies range from 70 to 90% of the theoretical maximum permitted by geometry (see Figure 5) and the silicon refractive index. The relative reflection efficiencies are close to the relative transmission efficiencies, indicating that reflection tests in the visible may be used as surrogate measurements to assess the quality of the grating without requiring a transmission measurement in the infrared. This is reasonable since the two measurements have comparable effective wavelengths and place roughly the same demands on the phase accuracy of the grating surface.

From the raw efficiency it is possible to obtain an estimate of the throughput of the grisms by assuming that they are outfitted with suitable anti-reflection coatings. We have assumed anti-reflection coatings with single-pass transmission equal to 95%, and computed the corresponding end-to-end throughput $\eta_T = \eta_{raw}(0.95)^2/[4n/(n+1)^2]^2$ at λ = 1.523 μm for grisms G3, G4, and G5. The results are listed in the final column of Table 3. Since grism G3 is intended to be used at moderate to high orders (m = 14 at λ = 8.0

μm to $m = 23$ at $\lambda = 4.9$ μm), η_T should be a reasonable estimate of the device throughput at the blaze wavelength. Somewhat higher throughput values are expected for grisms G4 and G5 because their geometric losses will be approximately one-third of that for G3. To estimate the throughput accurately for G4 and G5 at their blaze wavelengths requires a detailed electromagnetic calculation, since these devices are designed for use in low orders. We have not done that in this paper.

Reflection measurements also provide the (external) surface error plot shown in Figure 12. The surface plot is obtained using a Zygo interferometer by illuminating the grating in Littrow using collimated red HeNe light. As shown, the surface deviations are correlated into structures with spatial wavelengths approaching 10 mm or more. However, these deviations are small and the overall surface figure ($\varepsilon_{rms} < 10^{-2}$ waves rms at 632.8 nm) is excellent. Clearly, we can expect excellent performance of these grisms at their application wavelengths ($\lambda = 1$ to 40 μm).

6. Applications

The silicon grisms whose performance is described in Section 5 were designed to equip FORCAST, a cryogenic mid-infrared (5-40 μm) camera operating at liquid helium temperatures (4 K) with medium resolution spectroscopic capability[56,57] for use on NASA's airborne observatory.[58] All four of the gratings have been fabricated successfully and demonstrate optical performance at a level at which we can expect diffraction-limited performance over the 22 mm collimated beam of the instrument. Three of the four grating blanks have been successfully shaped into grisms, while the fourth is in the process of being shaped. To finish these devices requires the application

of suitable broadband antireflection (BBAR) coatings to the entrance and grating faces of each grism. This is challenging for the mid-infrared bands (17.1-28.1 μm and 28.6-37.4 μm) where the choice of available coating materials is limited and some development work is necessary. Initial development is encouraging and a suitable BBAR coating has been developed for the 4.9-8.1 μm wavelength range. This coating can be applied to Si grating facets with good uniformity, is mechanically robust, can survive multiple rapid thermal cycles between 300 K and 77 K, and raises the single-interface transmission from ~70% to better than 92% over this region.[53]

Grism G5 (δ = 6.16º, σ = 87 μm, right grism in center panel of Figure 4) is uncoated, but has been installed into FORCAST to assess its performance[59] in a cryogenic environment. An early atmospheric spectrum obtained with this grism is shown in Figure 13. Line fits to some of the deep absorption lines between 19 and 27 μm yield a resolution $\lambda/\Delta\lambda \approx 150$, limited by the slit. This verifies that the grism resolution is at least as great as this value.

These large, coarsely-ruled silicon grisms can be combined in cross-dispersed configurations to provide moderate resolution spectroscopy in the near-IR using all-transmissive optics. For example, the cross-dispersed configuration (G3 × G2) in FORCAST, provides a resolving power of R = 1200 with a coverage from 4.9 to 8.1 μm in a single exposure.

These grisms are developed in conjunction with silicon immersion gratings,[19] which require deeply blazed gratings and consequently thicker blanks. The optical tolerances on the groove placement are more stringent in the case of immersion gratings,

and we have developed methods that are compatible with production of both immersion and transmission devices. As a benefit, the optical performance for the grisms shown here exceeds what is required for applications.

This work is supported by NASA grants NAG5-8858, NRA 03-OSS-01 via the Astrobiology Science and Development (ASTID) program, and NNA 05CS83A via the NASA Astrobiology Institute (NAI), and by funding from the Universities Space Research Association (USRA 8500-98-008) and McDonald Observatory at the University of Texas at Austin. One of us (J. M.) acknowledges receipt of a NASA Graduate Research Program Fellowship (NGT5-137). Fabrication and testing of grating devices were made possible by facilities at the University of Texas at Austin, including the Center for Nano and Molecular Science and Technology (CNM), funded in part by the Welch Foundation, and the Microelectronics Research Center (MRC), funded in part by the National Science Foundation through the National Nanotechnology Infrastructure Network (NNIN). We thank R. Joyce, K. Hinkle, and G. Poczulp of National Optical Astronomy Observatory for interferometer measurements. We thank K. Allers, S. Joshi, and J. Zhou for assistance in process development, and T. Gaubert and W. Frey for help with AFM measurements. We also acknowledge helpful discussions with K. Ennico, A. Tokunaga, and P. Kuzmenko.

References

1. M. Nevière, "Electromagnetic study of transmission gratings" *Appl. Opt*. **30**, 4540-4547 (1991).
2. Carl Zeiss, "Grating Catalog", available at http://www.zeiss.de, 2004.
3. Newport Corporation, Diffraction Gratings Catalog, available from http://www.newport.com, 2005.
4. M. A. Davies, C. J. Evans, S. R. Patterson, R. Vohra, and B. C. Bergner, "Application of precision diamond machining to the manufacture of micro-photonics components," in *Lithographic and Micromachining Techniques for Optical Component Fabrication II*, E.-B. Kley and H. P. Herzig, eds., Proc. SPIE **5183**, 94-106 (2003).
5. P. J. Kuzmenko, "Prospects for machined immersion gratings in the near infrared and visible," in *Optomechanical Technologies for Astronomy*, E. Atad-Ettedgui, J. Antebi, and D. Lemke, eds., Proc. SPIE **6273**, 1181-1187 (2006).
6. H. U. Kaeufl, K. Kuehl, and S. Vogel, "Grisms from germanium/silicon for astronomical instruments," in *Infrared Astronomical Instrumentation*, A. M. Fowler, ed., Proc SPIE **3354**, 151-158 (1998).
7. N. Kobayashi, A. T. Tokunaga, H. Terada, M. Goto, M. Weber, R. Potter, P. M. Onaka, G. K. Ching, T. T. Young, K. Fletcher, D. Neil, L. Robertson, D. Cook, M. Imanishi, and D. W. Warren, "IRCS: infrared camera and spectrograph for the Subaru Telescope," in *Optical and IR Telescope Instrumentation and Detectors*, M. Iye and A. F. Moorwood, eds., Proc. SPIE **4008**, 1056-1066 (2000).
8. K. Matthews, and B. T. Soifer, "The near infrared camera on the W. M. Keck telescope," *Exp. Astr.* **3**, 77-84 (1994).

9. W. Freudling, "The NICMOS Grism Mode," in *The 1997 HST Calibration Workshop with a new generation of instruments*, S. Casertano, R. Jedrzejewski, C. D. Keyes, and M. Stevens, eds., (Space Telescope Science Institute, 1997), 207-216.

10. H.-G. Reimann, U. Weinert, and S. Wagner, "TIMMI2: a new MIR multimode instrument for ESO," in *Infrared Astronomical Instrumentation*, A. M. Fowler, ed., Proc. SPIE **3354**, 865-876 (1998).

11. L. K. Deutsch, J. L. Hora, J. D. Adams, and M. Kassis, "MIRSI: a Mid-InfraRed spectrometer and imager," in *Instrument Design and Performance for Optical/Infrared Ground-based Telescopes*, M. Iye and A. F. Moorwood, eds., Proc. SPIE **4841**, 106-116 (2003).

12. P. O. Lagage, J. W. Pel, M. Authier, J. Belorgey, A. Claret, C. Doucet, D. Dubreuil, G. Durand, G. E. Elswijk, P. Giradot, H. U. Käufl, G. Kroes, M. Lortholary, Y. Lussignol, M. Marchesi, E. Pantin, R. Peletier, J.-F. Pirard, J. Pragt, Y. Rio, T. Schoenmaker, R. Siebenmorgen, A. Silber, A. Smette, M. Sterzik, and C. Veyssiere, "Successful Commissioning of VISIR: the mid-infrared VLT instrument," *The Messenger* **117**, 12-16 (2004).

13. P. Philippe, S. Valette, O. Mata Mendez, and D. Maystre, "Wavelength demultiplexer using echelette gratings on silicon substrate," *Appl. Opt.* **24**, 1006-1011 (1985).

14. Zhao, F., Qiao, J., Deng, X., Zou, J., Guo, B., Collins, R., Villavicencio, V., Chang, K. K., Horwitz, J. W., Morey, B., and Chen, R. T. "Reliable grating-based wavelength division (de)multiplexers for optical networks." *Opt. Eng.* 40 (2001): 1204-1211.

15. G. J. Tearney, R. H. Webb, and B. E. Bouma, "Spectrally encoded confocal microscopy," *Opt. Lett.* **23**, 1152-1154 (1998).

16. C. Pitris, B. E. Bouma, M. Shiskov, and G. J. Tearney, "A grism-based probe for spectrally encoded confocal microscopy," *Opt. Express* **11**, 120-124 (2003).

17. P. Tournois, "New diffraction grating pair with very linear dispersion for laser pulse compression," *Electron. Lett.* **29**, 1414-1415 (1993).

18. S. Kane, and J. Squier, "Grism-pair stretcher-compressor system for simultaneous second- and third-order dispersion compensation in chirped pulse amplification," *J. Opt. Sci. Am. B* **14**, 661-665 (1997).

19. J. P. Marsh, D. J. Mar, and D. T. Jaffe, "Production and evaluation of silicon immersion gratings for infrared astronomy," submitted to *Appl. Opt.* (2006).

20. H. Y. Fan, and M. Becker, "Infra-red absorption of silicon," *Phys. Rev.* **78**, 178 (1950).

21. W. Spitzer, and H. Y. Fan, "Infrared absorption in n-type silicon," *Phys. Rev.* **108**, 268 (1957).

22. W. R. Runyan, *Silicon Semiconductor Technology*, (McGraw-Hill, 1965).

23. D. K. Schroder, R. N. Thomas, and J. C. Swartz, "Free carrier absorption in silicon," *IEEE Journal of Solid-State Circuits* **13**, 180-187 (1978).

24. R. J. Collins, and H. Y. Fan, "Infrared lattice absorption bands in germanium, silicon, and diamond," *Phys. Rev.* **93**, 674-678 (1954).

25. W. Kaiser, P. H. Keck, and C. F. Lange, "Infrared absorption and oxygen content in silicon and germanium," *Phys. Rev.* **101**, 1264-1268 (1956).

26. H. J. Hrostowski, and R. H. Kaiser, "Infrared absoprtion of oxygen in silicon," *Phys. Rev.* **107**, 966-972 (1957).

27. F. M. Livingston, S. Messoloras, R. C. Newman, B. C. Pike, R. J. Stewart, M. J. Binns, W. P. Brown, and J. G. Wilkes, "An infrared and neutron scattering analysis of the precipitation of oxygen in dislocation-free silicon," *J. Phys. C* **17**, 6253-6276 (1984).

28. R. C. Lord, "Far infrared transmission of silicon and germanium," *Phys. Rev.* **85**, 140-141 (1952).

29. W. C. Dash, and R. Newman, "Intrinsic optical absorption in single-crystal germanium and silicon at 77K and 300K," *Phys. Rev.* **99**, 1151-1155 (1955).

30. G. G. MacFarlane, T. P. McLean, J. E. Quarrington, and V. Roberts, "Fine structure in the absorption-edge spectrum of Si," *Phys. Rev.* **111**, 1245-1254 (1958).

31. T. A. Kwa, P. J. French, R. F. Wolffenbuttel, P. M. Sarro, L. Hellemans, and J. Snauwaert, "Anisotropically etched silicon mirrors for optical sensor applications," *J. Electrochem. Soc.* **142**, 1226-1233 (1995).

32. C. Merveille, "Surface quality of {111} side-walls in KOH-etched cavities," *Sensors and Actuators A* **60**, 244-248 (1997).

33. P. J. Kuzmenko, and D. R. Ciarlo, "Improving the optical performance of etched silicon gratings," in *Infrared Astronomical Instrumentation*, A. M. Fowler, ed., Proc. SPIE **3354**, 357-367 (1998).

34. B. J. Frey, D. B. Leviton, and T. J. Madison, "Temperature-dependent refractive index of silicon and germanium," in *Optomechanical Technologies for Astronomy*, E. Atad-Ettedgui, J. Antebi, and D. Lemke, eds., Proc. SPIE **6273**, 62732J (2006).

35. L. J. Neuringer, "Effect of pressure on the infrared absorption of semiconductors," *Phys. Rev.* **113**, 1495-1503 (1959).

36. L. F. Thompson, C. G. Willson, and M. J. Bowden, eds., *Introduction to Microlithography*, *2nd ed.*, (Oxford University Press, 1994).

37. D. B. Lee, "Anisotropic etching of silicon," *J. Appl. Phys.* **40**, 4569-4574 (1969).

38. H. Seidel, L. Csepregi, A. Heuberger, and H. Baumgartel, "Anisotropic etching of crystalline silicon in alkaline solutions--part I. orientation dependence and behavior of passivation layers," *J. Electrochem. Soc.* **187**, 3612-3626 (1990).

39. W. T. Tsang and S. Wang, "Preferentially etched diffraction gratings in silicon" *J. Appl . Phys.* **46**, 2163-2166 (1975).

40. G. Wiedemann, and D. E. Jennings, "Immersion grating for infrared astronomy," *Appl. Opt.* **32**, 1176 (1993).

41. P. J. Kuzmenko, D. R. Ciarlo, and C. G. Stevens, "Fabrication and testing of a silicon immersion grating for infrared spectroscopy," in *Optical Spectroscopic Techniques and Instrumentation for Atmospheric and Space Research*, J. Wang and P. B. Hays, eds., Proc. SPIE **2266**, 566-577 (1994).

42. U. U. Graf, D. T. Jaffe, E. J. Kim, J. H. Lacy, H. Ling, J. T. Moore, and G. Rebeiz, "Fabrication and evaluation of an etched infrared diffraction grating," *Appl. Opt.* **33**, 96-102 (1994).

43. L. D. Keller, D. T. Jaffe, O. A. Ershov, T. Benedict, and U. U. Graf, "Fabrication and testing of chemically micromachined silicon echelle gratings," *Appl. Opt.* **39**, 1094-1105 (2000).

44. F. Vitali, E. Cianci, D. Lorenzetti, V. Foglietti, A. Notargiacomo, E. Giovine, and E. Oliva, “Silicon grisms for high-resolution spectroscopy in the near infrared,” in *Optical and IR Telescope Instrumentation and Detectors*, M. Iye and A. F. Moorwood, eds., Proc. SPIE **4008**, 1383-1394 (2000).

45. O. A. Ershov, D. T. Jaffe, J. P. Marsh, and L. D. Keller, "Production of high-order micromachined silicon echelles on optically flat substrates," in *Lithographic and Micromachining Techniques for Optical Component Fabrication*, E.-B. Kley and H. P. Herzig, eds., Proc. SPIE **4440**, 301-308 (2001).

46. F. Vitali, E. Cianci, V. Foglietti, and D. Lorenzetti, "Fabrication of silicon grisms," in *Specialized Optical Developments in Astronomy*, E. Atad-Ettedgui and S. D'Odorico, eds., Proc. SPIE **4842**, 274-281 (2003).

47. O. A. Ershov, J. P. Marsh, K. N. Allers, and D. T. Jaffe, "Infrared grisms using anisotropic etching of silicon to produce a highly asymmetric groove profile," in *IR Space Telescopes and Instruments*, J. C. Mather, ed., Proc. SPIE **4850**, 805-812 (2003).

48. J. Ge, D. L. McDavitt, S. Miller, J. L. Bernecker, A. Chakraborty, and J. Wang, "Breakthroughs in silicon grism and immersion grating technology at Penn State," in *Instrument Design and Performance for Optical/Infrared Ground-based Telescopes*, M. Iye and A. F. Moorwood, eds., Proc SPIE **4841**, 1006-1015 (2003).

49. D. McDavitt, J. Ge, S. Miller, and J. Wang, "Silicon immersion gratings for very high resolution infrared spectroscopy," in *Optical Fabrication, Metrology, and Material Advancements for Telescopes*, E. Atad-Ettedgui and P. Dierickx, eds., Proc. SPIE **5494**, 536-544 (2004).

50. S. S. Tan, M. L. Reed, H. Han, and R. Boudreau, "Mechanisms of etch hillock formation," *J. Microelectromech. Sys.* **5**, 66-72 (1996).

51. G. Nanz, and L. E. Camilletti, "Modeling of Chemical-Mechanical Polishing: a Review," *IEEE Trans. Semiconductor Manufacturing* **8**, 382-389 (1995).

52. D. T. Jaffe, L. D. Keller, and O. A. Ershov, "Micromachined silicon diffraction gratings for infrared spectroscopy," in *Infrared Astronomical Instrumentation*, A. M. Fowler, ed., Proc. SPIE **3354**, 201-212 (1998).

53. D. J. Mar, J. P. Marsh, D. T. Jaffe, L. D. Keller, and K. A. Ennico, "Performance of large chemically etched silicon grisms for infrared spectroscopy," in *Ground-based and Airborne Instrumentation for Astronomy*, I. S. McLean and M. Iye, eds., Proc. SPIE **6269**, 62695R (2006).

54. S. A. Campbell, K. Cooper, L. Dixon, R. Earwaker, S. N. Port, and D. J. Schiffrin, "Inhibition of pyramid formation in the etching of Si p(100) in aqueous potassium hydroxide-isopropanol," *J. Micromech. Microeng.* **5**, 209-218 (1995).

55. J. P. Marsh, O. A. Ershov, and D. T. Jaffe, "Silicon grisms and immersion gratings produced by anisotropic etching: testing and analysis," in *IR Space Telescopes and Instruments*, J. C. Mather, ed., Proc. SPIE **4850**, 797-804 (2003).

56. L. D. Keller, T. L. Herter, G. J. Stacey, G. E. Gull, B. Pirger, J. Schoenwald, H. Bowmann, and T. Nikola, "FORCAST: a facility 5-40 micron camera for SOFIA," in *Airborne Telescope Systems*, R. K. Melugin and H.-P. Roeser, eds., Proc. SPIE **4014**, 86-97 (2000).

57. L. D. Keller, T. L. Herter, G. J. Stacey, G. E. Gull, J. Schoenwald, B. Pirger, and T. Nikola, "FORCAST: the faint object infrared camera for the SOFIA telescope," in *Airborne Telescope Systems II*, R. K. Melugin and H.-P. Roeser, eds., Proc. SPIE **4857**, 29-36 (2003).

58. E. F. Erickson and J. A. Davidson, "SOFIA: the future of airborne astronomy," *ASP Conference Series*, **73**, 707-773 (1995).

59. K. A. Ennico, L. D. Keller, D. J. Mar, T. L. Herter, D. T. Jaffe, J. D. Adams, and T. P. Greene, "Grism performance for mid-IR (5-40 micron) spectroscopy", in *Ground-based and*

Airborne Instrumentation for Astronomy, I. S. McLean and M. Iye, eds., Proc. SPIE **6269**, 62691Q (2006).

60. N. Ebizuka, M. Iye, and T. Sasaki, "Optically anisotropic crystalline grisms for astronomical spectrographs," *Appl. Opt.* **37**, 1236-1242 (1998).
61. J. T. Rayner, "Evaluation of a solid KRS-5 grism for infrared astronomy," in *Infrared Astronomical Instrumentation*, A. M. Fowler, ed., Proc. SPIE **3354**, 289-294 (1998).

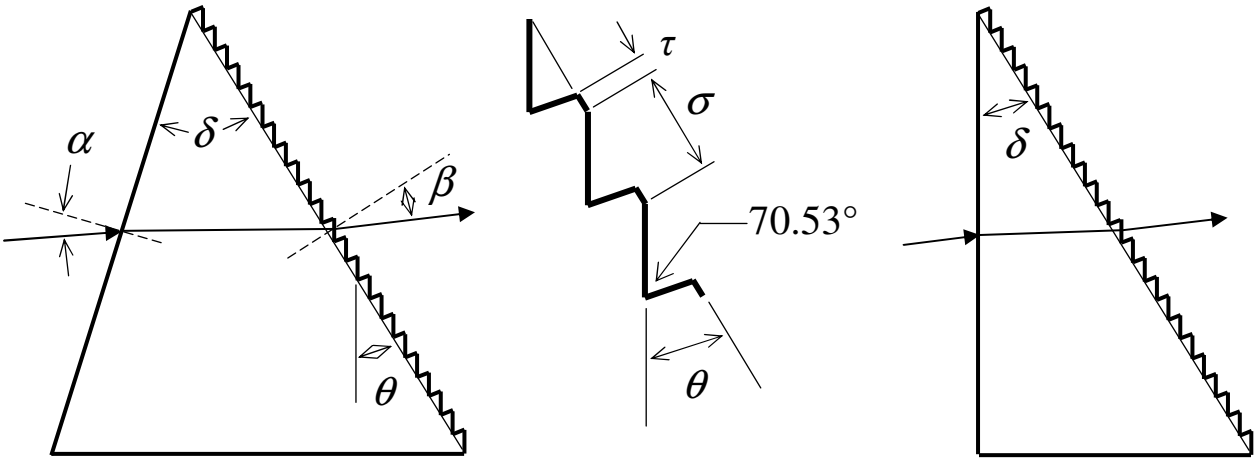

Figure 1. *Left*: Schematic diagram of a grism with wedge angle δ and blaze angle θ. The blaze angle is measured between the groove facet and the grating surface. The incident angle α and diffracted angle β are measured with respect to the corresponding normals at the surfaces of the grism and the sign convention is that both angles are positive in the sense drawn. *Center*: Detail of a silicon grating surface showing groove period σ. The plane of the figure is the (110) crystal plane. For silicon material, the facets are adjacent {111} crystal planes and the valley angle measures 70.53°. For the situation in which the facets are non-adjacent, the valley angle is 109.47° (not shown here, but see Ref. 47). As shown, for acute valley angles, the projection along the optical axis of the unused facet and the groove top τ partially coincide, reducing the geometric transmission loss. *Right*: For most of the grisms that we have fabricated, the blazed facets are parallel to the entrance surface so that $\theta = \delta$.

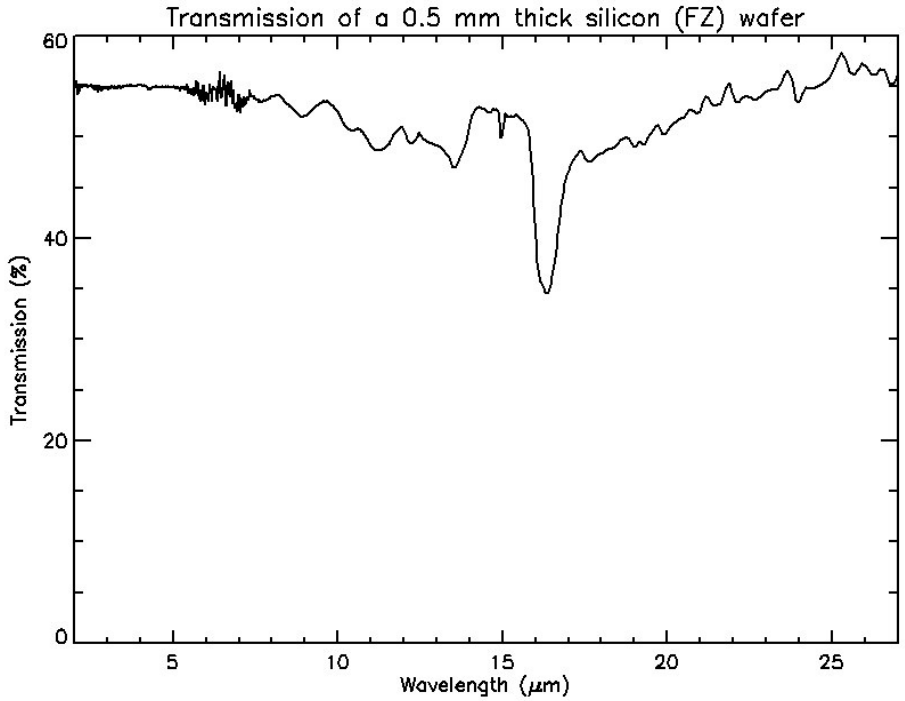

Figure 2. Infrared transmission from 3 to 27 μm of a 0.5 mm thick sample of high-purity float-zone Si, measured at 300 K using Fourier Transform Infrared Spectroscopy (FTIR). Except for lattice absorption near 16 μm, the sample has good transparency. The oxygen absorption features[25-27] at 9 and 19 μm are not very prominent but will still cause a significant drop in transmission for thicker devices. The reflectivity of a single silicon surface is 30% at 3-5 μm and the resulting transmission for an uncoated substrate is 55% when contributions from all re-reflected light is accounted for.

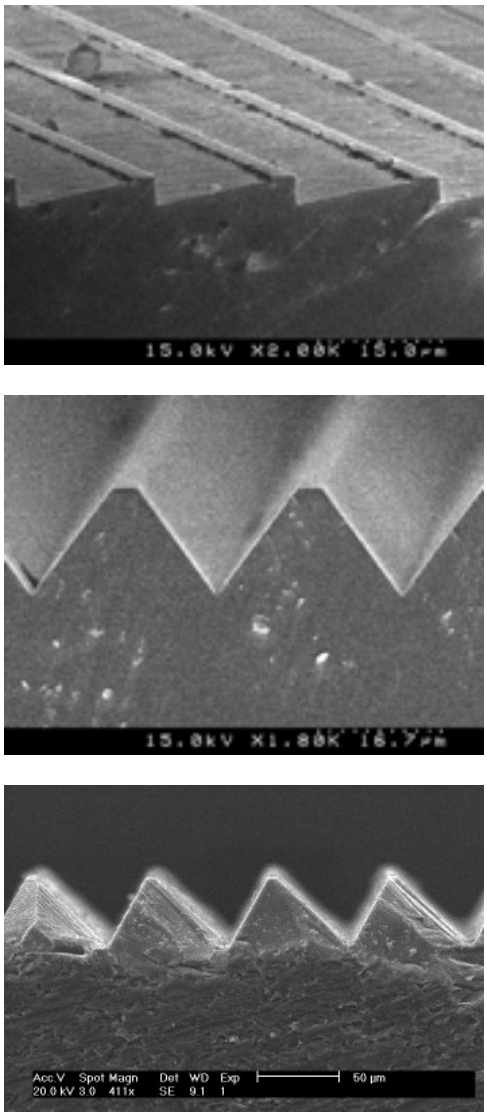

Figure 3. Scanning electron micrographs of gratings with different blaze angles δ and groove constants σ: (a) δ = 6.16° and σ = 25 µm, (b) δ = 54.7° and σ = 25 µm, and (c) δ = 63.4° and σ = 80 µm. The grooves in (b) are symmetric with respect to the top surface. In all three panels the sloping faces are very nearly parallel to {111} crystal planes. From surface profilometry, we obtain valley angles of 72.12° with a measurement uncertainty of 0.05°. The small difference between this value and the $\cos^{-1}(1/3)$ = 70.53° angle between nearby {111} planes reflects undercutting arising from the finite etch anisotropy.[19] The top and center panels are taken from Ref. 47.

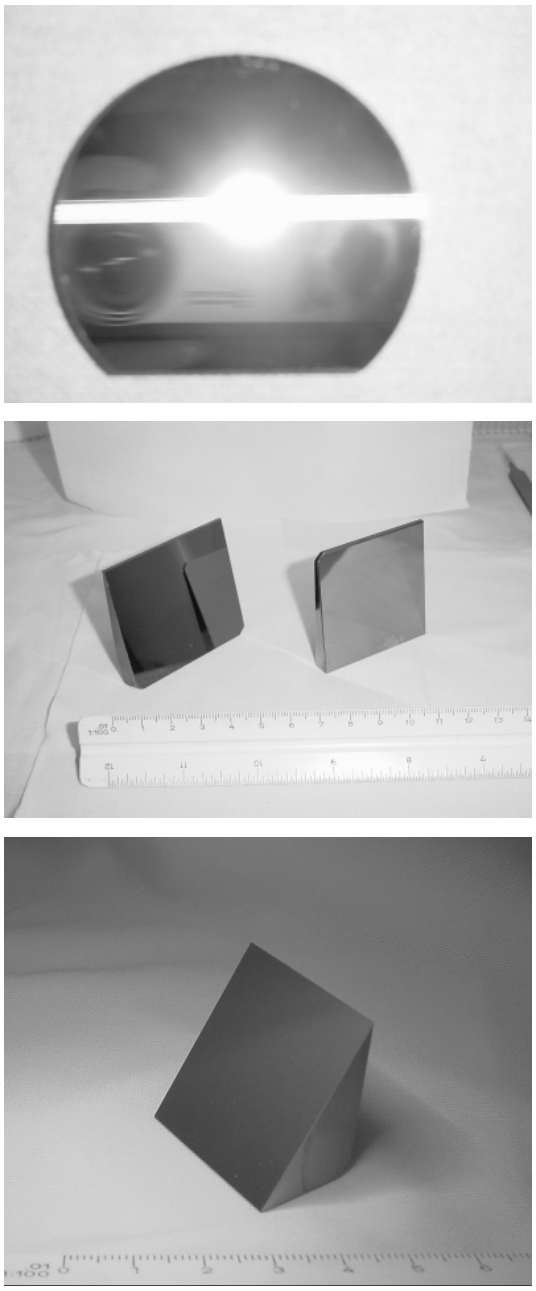

Figure 4. Images taken of silicon gratings after wet etching, before (top) and after (middle, bottom) devices have been shaped into wedges. The top photograph is taken in Littrow (note the image of the camera) and the camera flash has been dispersed left-right by the grating. The major (horizontal) axis measures 76 mm. For the grisms in the middle and bottom images, the wedge angles δ are clearly visible and the ruled surfaces are towards the viewer. In the middle image, the polished entrance face of the grism on the right (grating area 51 mm × 50 mm) is seen reflected in the ruled surface of the grism on the left (grating area 51 mm × 57 mm). In the bottom image, the corresponding area is 37 mm × 32 mm. Only commercially-available anti-reflection coatings are needed to complete the wedged grisms. From top to bottom, these four gratings are G2, G5 and G4, and G3 as listed in Table 2.

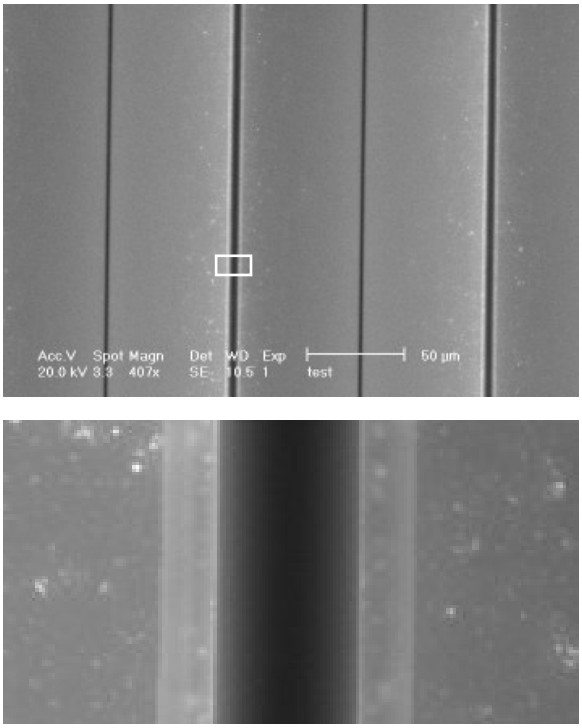

Figure 5. SEM micrographs of a symmetric (θ = 54.7°) grating immediately after etching in potassium hydroxide, viewed normal to the grating face. The grating period is σ = 142 µm. The thin dark vertical lines are the groove tops and valleys. The detailed view at bottom corresponds to the white box inset in the top panel. One can see the strip of silicon nitride covering the darker groove top and overhanging by approximately 2 µm at each edge of the groove top. The silicon nitride and the silicon hydroxide precipitates are effectively removed by washing the part in hot (140°C) ortho-phosphoric acid.

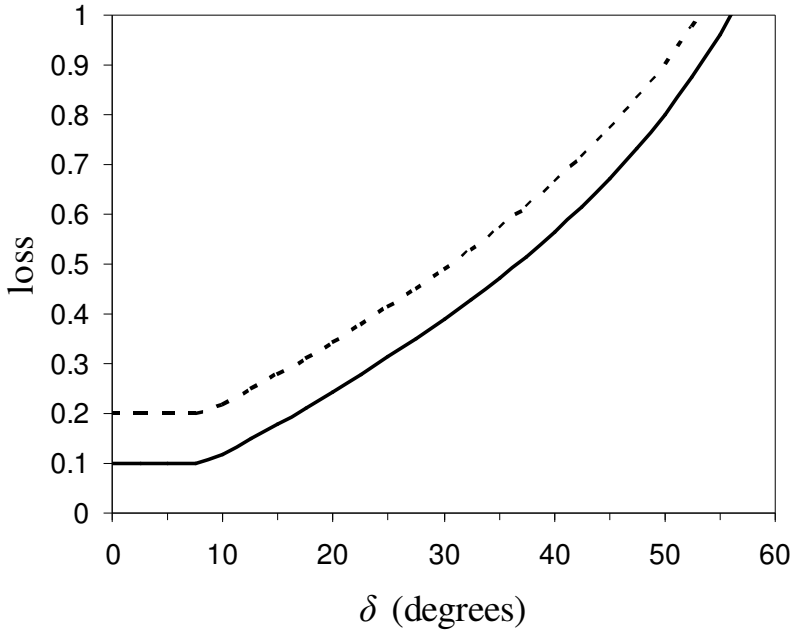

Figure 6. Geometric loss as a function of grism angle δ, for $\alpha = 0$ and fixed valley angles of 70.53° (solid curve) and 109.47° (dotted curve) between the facets of the grooves, for $t/\sigma = 5\%$. These curves include both the loss due to the unused area of the beam and the accompanying loss due to diffraction into undesired orders. For shallow angle grisms ($\delta < 8°$), the groove top dominates the shadowing and the curves are flat.

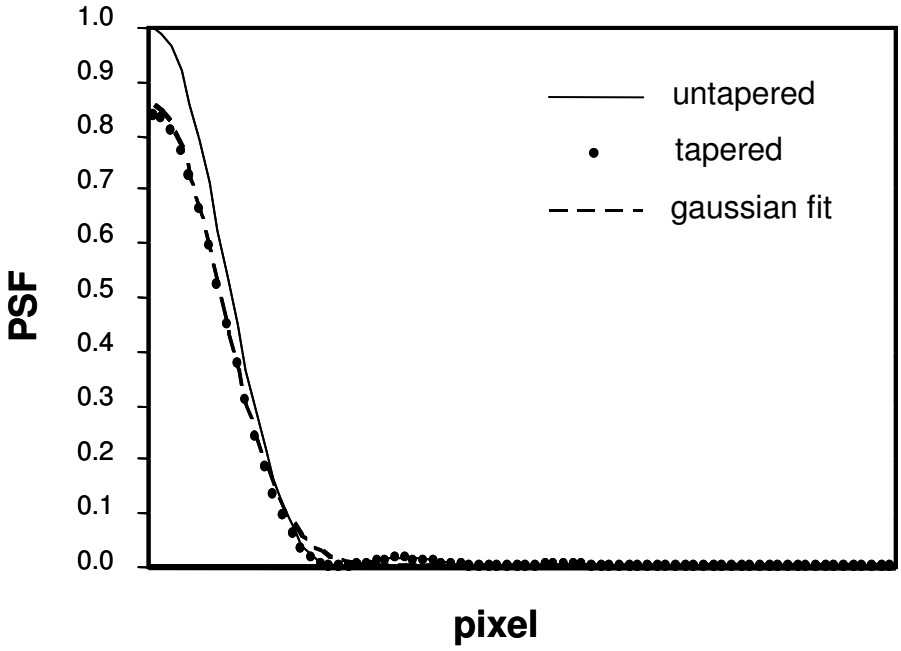

Figure 7. Computed point spread function for transmission of a 25 mm diameter collimated beam through a silicon grism with $\delta = 32.6°$, showing effect of absorption and tapering due to differential absorption in the silicon across the beam. The untapered (line) and tapered (dots) curves are calculated for Si absorption coefficients $\alpha = 0$ cm^{-1} and 0.2 cm^{-1} respectively. As shown, the main effect of absorption is to attenuate the intensity across the beam: the peak maximum has dropped by 16%. The width of the best Gaussian fit to the tapered profile (dotted line) has increased only slightly (approximately 0.1%) over the width of the best fit (not shown) to the untapered profile (solid line). At the center of the beam, the path length in the Si is 0.8 cm.

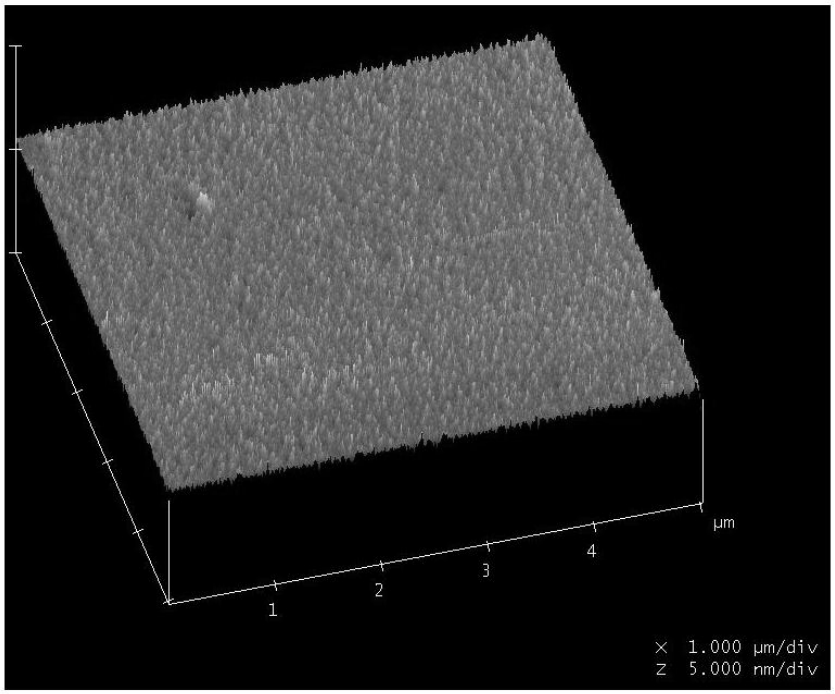

Figure 8. Three-dimensional representation of the surface of a groove facet obtained using an atomic force microscope (AFM). The field measures 5 µm × 5 µm. The surface roughness over this area is measured to be 1.7 nm rms. The roughness is unchanged across the entire facet. The bump at the upper left is 4 nm in height. The scan is taken from an offcut of grism G2 ($\delta = 6.16°$ and $\sigma = 25$ µm, see Table 2).

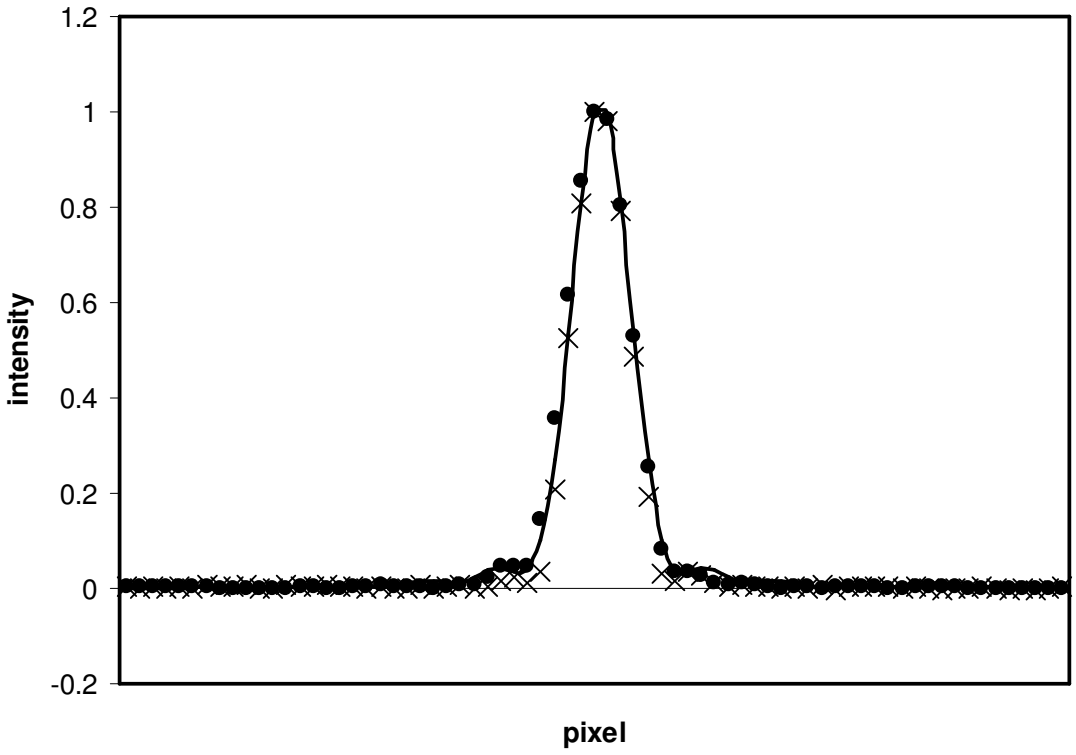

Figure 9. Normalized one-dimensional point spread function (PSF) taken in transmission using a 10 mm diameter beam with λ = 1523 nm. Filled circles show the PSF measured for grism G3, and is a spectrum of the brightest diffraction order shown in the first plot of Figure 10. The horizontal axis is the dispersion direction. Crosses show the corresponding data taken from a Si reference mirror. Both the data from the grism and the mirror nearly coincide with the theoretical curve (solid line) calculated for a 10 mm circular aperture, indicating diffraction-limited performance. The full width of the profile corresponds to $R = \lambda/\Delta\lambda = 1.0 \times 10^4$.

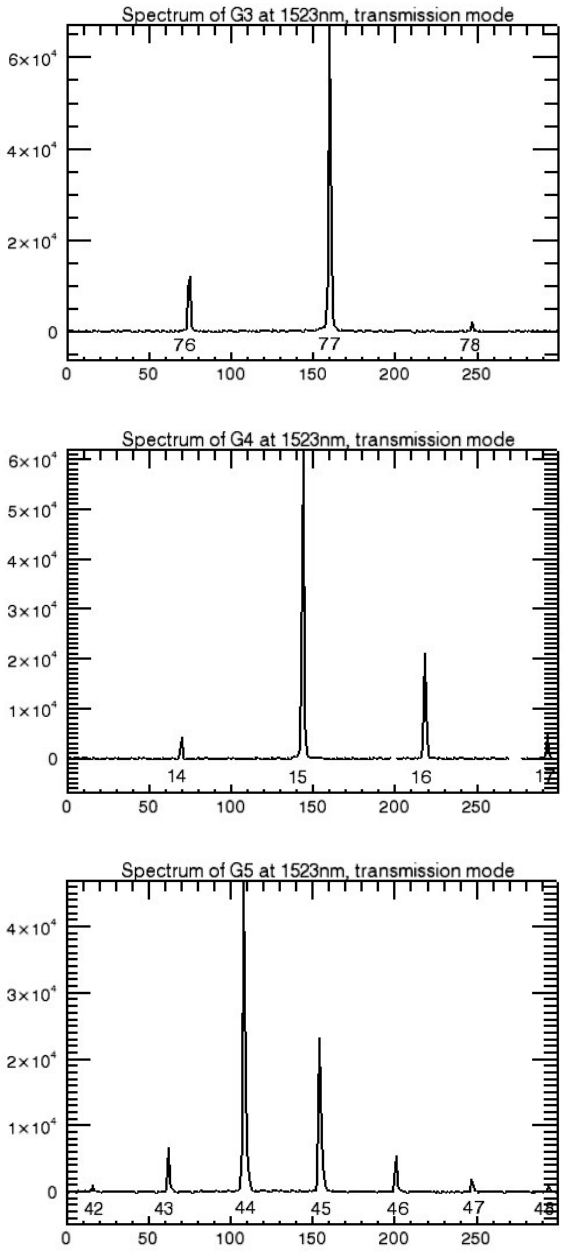

Figure 10. Monochromatic transmission spectra of grisms G3 (top), G4 (center), and G5 (bottom), taken using a 10 mm diameter collimated beam with λ = 1523 nm. Order numbers are indicated near the bottom of each peak.

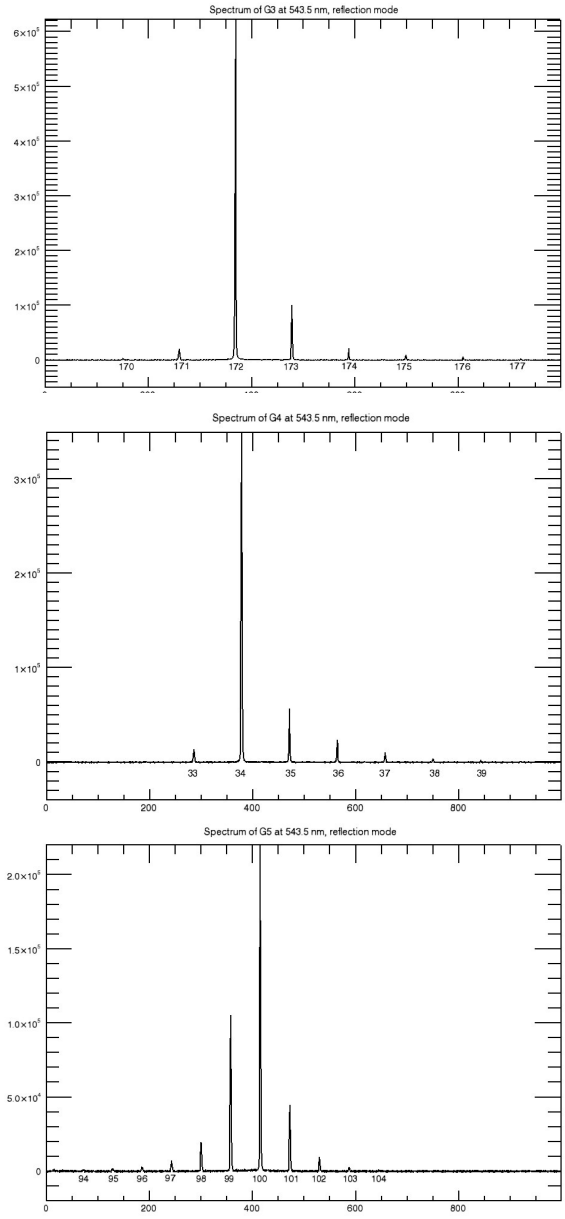

Figure 11. Monochromatic reflection spectra of grisms G3 (top), G4 (middle), and G5 (bottom), taken using a 23 mm (G3) or 25 mm (G4, G5) diameter collimated beam with λ = 543.5 nm. Order numbers are indicated near the bottom of each peak. The panels correspond to those in Figure 10.

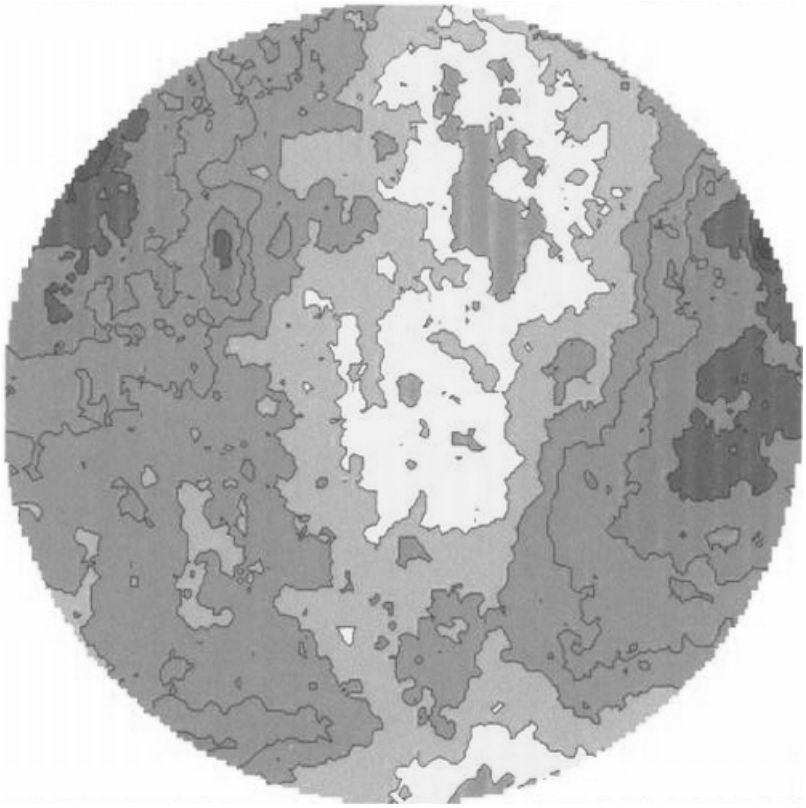

Figure 12. Surface error plot of grism G2 (σ = 25 μm and δ = 6.16°), as obtained from front-surface reflectivity measurements using λ = 632.8 nm laser light. Each contour represents approximately 1/150 of a wave. The rms deviation over the indicated 25 mm diameter aperture is approximately 10^{-2} waves.

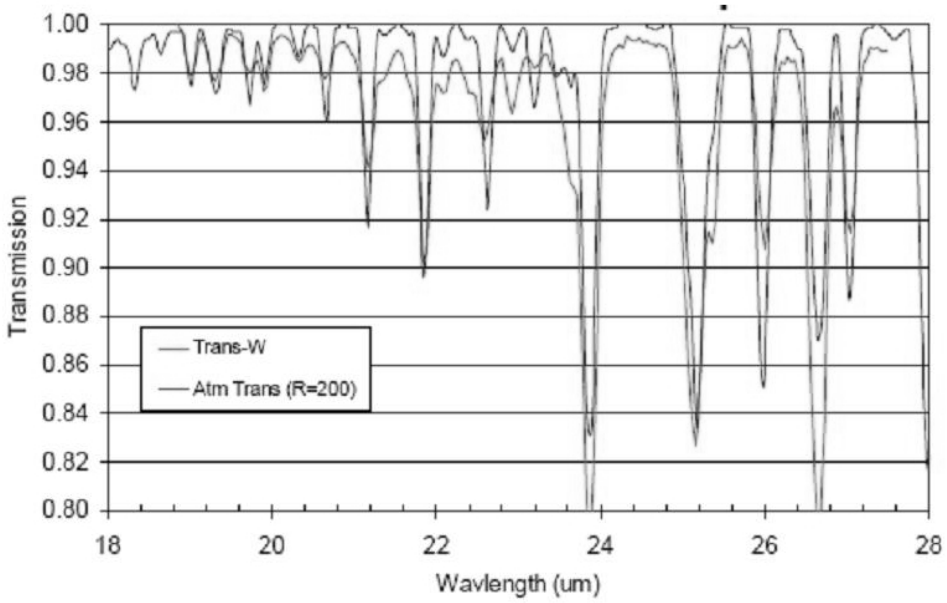

Figure 13. Grism lab transmission spectrum (red) for a 2.9 pixel slit showing water absorption lines taken using grism G5. Shown in blue is an ATRAN calculation for atmospheric transmission expected from SOFIA for 7.3 microns of precipitable water vapor and 45 degrees from zenith at a spectral resolution of 200. The measurement resolution is limited by the slit. For additional details, see Ref. 59.

Table 1. Potential infrared grism materials and properties.

Reference	Material	Index[a]	Grism type[b]	Bandpass (microns)	Comment
Carl Zeiss Inc. 2004)	resin / BK-7	1.5 / 1.5	replica, hybrid	0.3 - 2.5	
	CaF_2	1.4	ruled		
Rayner (1998)	KRS-5	2.4	ruled	0.5 - 35	
Ebizuka, Iye, and Sasaki (1998)	$LiNbO_3$ / ZnS	2.2 / 2.2	etched, hybrid	0.35 - 4.6	birefringent
	ZnSe	2.5	ruled	0.6 - 21	brittle, low efficiency
	Si	3.4	etched	1.2 - 15, 17 - 35	monolithic
Kaüfl, Kühl and Vogel (1998)	Si / Ge	3.4 / 4.0	ruled, hybrid	1.8 - 23	

[a]The indices of refraction are for comparison purposes only, since the actual index varies with wavelength and temperature.

[b]Hybrid grisms are formed by fabricating the grating on a thin substrate and then attaching it to a thicker prism substrate (e.g. resin on BK-7).

Table 2. Summary of design parameters for silicon grism devices shown in this paper. See Figure 1 for the definitions of the various dimensions.

Grating	δ (°)	θ (°)	σ (µm)	t (µm)	m	λ_{blaze} (µm)
G2	6.16	6.16	25	2.5	1	6.6
G3	32.6	32.6	87	6.0	14 - 23	5.0 - 8.2
G4	6.16	6.16	87	6.0	1	22.8
G5	11.07	11.07	142	10.0	2	33.3

Table 3. Efficiencies for the three grisms whose transmission spectra are shown in Figure 10. The raw efficiency η_{raw} measures the ratio of transmitted to incident light at λ = 1523 nm. The groove efficiency η_{groove} corrects for expected Fresnel (the grisms are uncoated) and geometric (see Figures 1 and 6) losses and reflects the overall quality of the fabricated gratings. The values greater than 100% are consistent with groove efficiencies ~100% in the transmission mode (our estimated systematic errors were 10-15%). Another measurement of the groove efficiency is obtained using reflected light at λ = 543.5 nm (Figure 11), similarly corrected for Fresnel and geometric losses. The last column is the expected transmission throughput at λ = 1523 nm inferred from η_{raw} at 1523 nm, assuming that both the entrance and grating faces of the grism have been coated with an antireflection coating whose single-pass reflectivity is 5%.

Grism	η_{raw} (%) (1523 nm)	η_{groove} (%) (1523 nm)	η_{raw} (%) (543.5 nm)	η_{groove} (%) (543.5 nm)	η_T (%) (1523 nm)
G3	31	109	78	91	58
G4	44	104	73	85	82
G5	48	114	65	76	89